

Valence-Regulated Metal Doping of Mixed-Halide Perovskites to Modulate Phase Segregation and Solar Cell Performance

Long Hu,[▼] Xinwei Guan,[▼] Tao Wan,[▼] Chun-Ho Lin, Shanqin Liu, Renbo Zhu, Weijian Chen, Yin Yao, Chien-Yu Huang, Lin Yuan, Shamim Shahrokhi, Dewei Chu,* Claudio Cazorla,* Junfeng Chen, Jack Yang,* Jiabao Yi, Shujuan Huang,* and Tom Wu*



Cite This: *ACS Energy Lett.* 2022, 7, 4150–4160



Read Online

ACCESS |



Metrics & More

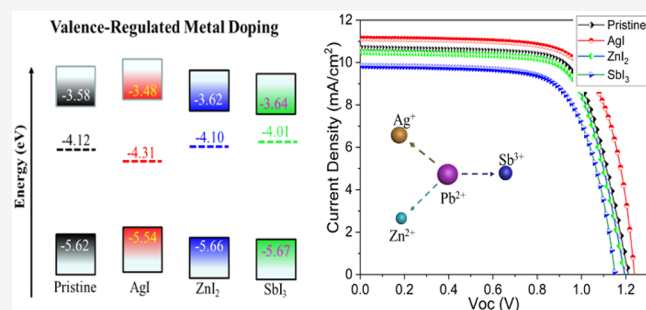


Article Recommendations



Supporting Information

ABSTRACT: Electronic doping is a promising approach to modulating the optoelectronic properties of semiconductors, but its effect on optoelectronic behaviors of halide perovskites remains controversial. Here, we comprehensively investigate the impact of Pb substitution in n-type CsPbI₂Br₂ perovskite by utilizing monovalent Ag, divalent Zn, and trivalent Sb. Our findings reveal that the trap densities in doped CsPbI₂Br₂ films are in the order of Ag < Zn < Sb. Compared with the pristine CsPbI₂Br₂, the Ag-doped perovskite features a significantly reduced phase separation; however, the Sb doping accelerates halide segregation, and Zn exerts a negligible influence. The p-doping effect from monovalent Ag can shift the Fermi level of CsPbI₂Br₂ toward the intrinsic midgap, which helps prevent the formation of ionic defects and reduce the migration of halide ions in the perovskite lattice. Through combining the density functional theory simulation, this study discloses the correlation between valence-controlled metal doping and phase segregation, providing a guideline for judiciously doping mixed-halide perovskites for optoelectronic applications.



Phase segregation in mixed halide perovskites was first reported by Hoke et al. in 2015, where the homogeneous mixed-halide perovskite film with uniform bandgap could segregate to small-bandgap I-rich domains and large-bandgap Br-rich domains under continuous light illumination.¹ It was observed that I-rich domains aggregate in grain boundaries due to halide ion movement, which results in a red-shift of photoluminescence (PL) emission.^{2–7} Up to date, many strategies have been adopted to suppress the phase segregation, such as controlling the crystal grain size,^{2,8,9} managing defect density,^{10–14} and engineering the composition of mixed halide perovskite films.^{15–17} Meanwhile, electronic doping has been extensively employed to modulate the optoelectronic properties of semiconductors via directly modulating the majority carrier property (p-type, intrinsic, or n-type) and carrier density;¹⁸ however, its effect in halide perovskites remains controversial, and the associated influence on phase segregation behaviors is still unclear.¹⁹

Very recently, all-inorganic mixed halide perovskites CsPbI_{3-x}Br_x have emerged as promising candidates for both single-junction and tandem solar cell applications owing to their excellent thermal endurance compared with organic–

inorganic hybrid halide perovskites.^{20–25} Among the family of inorganic CsPbI_{3-x}Br_x perovskites, CsPbI₂Br₂ is attracting increasing attention for top cells in tandem devices due to its desirable bandgap of 2.0 eV and superior air stability.^{26–28} To further optimize the performance of CsPbI₂Br₂, intentional metal doping can be a powerful strategy since it can modify the optoelectronic properties, thereby affecting the charge recombination and transportation in optoelectronic devices.^{22,29–34} However, metal doping with different valence states in CsPbI₂Br₂ perovskite has not been systematically investigated so far, and its impact on halide phase segregation is unknown, which can critically influence the optoelectronic device performance and photostability.

Received: September 8, 2022

Accepted: October 24, 2022

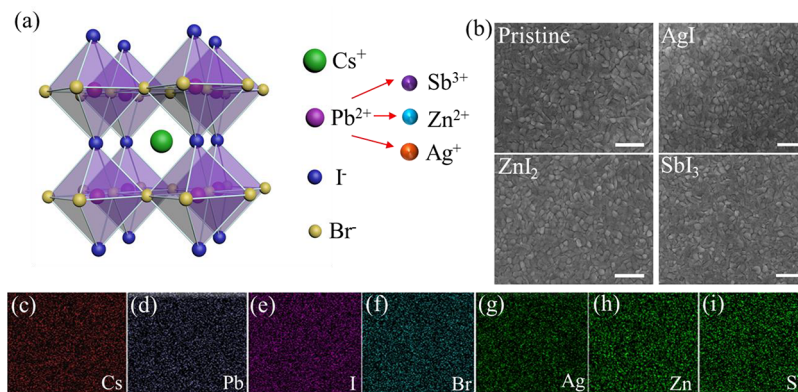


Figure 1. (a) Schematic diagram of cubic CsPbIBr_2 with atomic coordination of Cs, Pb, Br and I elements; the proposed substitution of Pb^{2+} cation by valence-controlled Ag^+ , Zn^{2+} and Sb^{3+} cations. (b) Top-view SEM images of the pristine, AgI -, ZnI_2 - and SbI_3 -doped CsPbIBr_2 perovskite films (Scale bar: 100 nm). EDX mapping of (c) Cs, (d) Pb, (e) I and (f) Br elements for the pristine CsPbIBr_2 film, as well as mapping of (g) Ag, (h) Zn, and (i) Sb elements for the doped CsPbIBr_2 films (area scale: $5 \times 5 \mu\text{m}$).

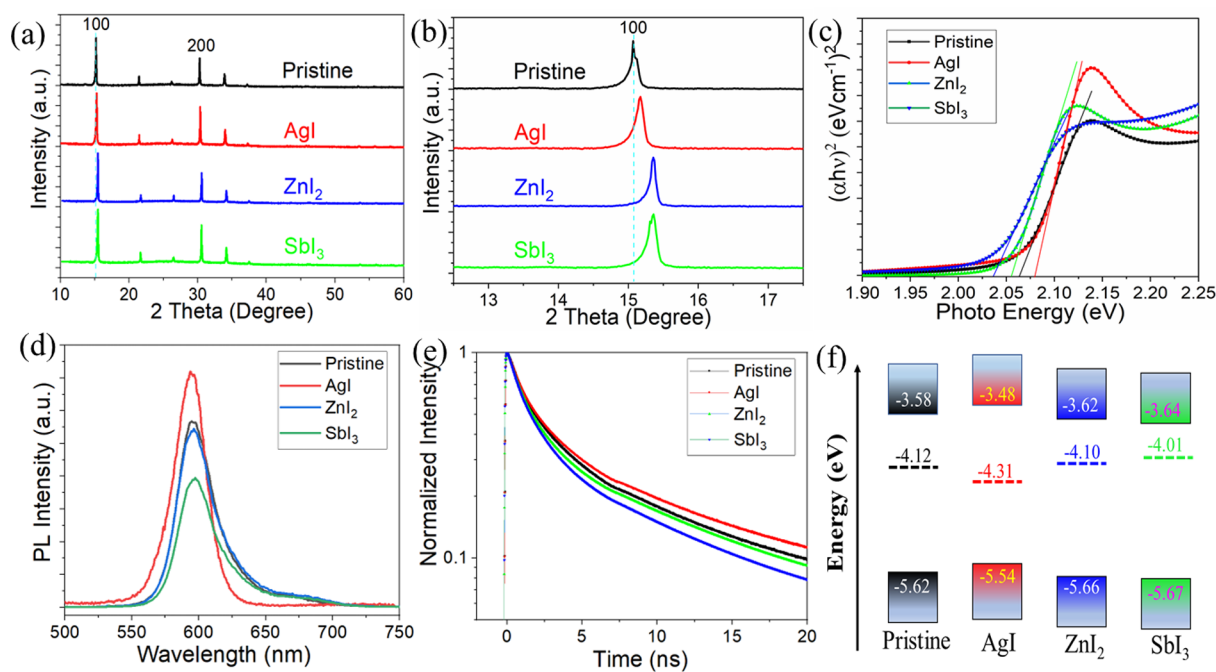


Figure 2. (a and b) XRD patterns, (c) calculated bandgaps, (d) steady-state PL and (e) TRPL decay of pristine, AgI -, ZnI_2 - and SbI_3 -doped CsPbIBr_2 films, (f) energy level of pristine, AgI -, ZnI_2 - and SbI_3 -doped CsPbIBr_2 films.

Here, we systematically investigated the effect of extrinsic metal doping on optoelectronic properties, phase segregation behaviors, and solar cell photostability based on CsPbIBr_2 perovskites. The substitution of the Pb site by valence-controlled metals (i.e., Ag, Zn, and Sb) was found to lead to different doping types and optoelectronic properties. In contrast to the divalent Zn, which leads to intrinsic doping and phase segregation behavior that is comparable to the undoped counterpart, the trivalent Sb produces n-type doping, increases trap states, and accelerates phase segregation. Most importantly, the p-type doping by monovalent Ag can successively shift the Fermi level of CsPbIBr_2 toward the middle of the bandgap, thereby suppressing the formation of defect trap states and diminishing unfavorable phase segregation. Photovoltaic cells were further fabricated based on CsPbIBr_2 perovskite films with different doping types, which confirmed that the effect of metal doping significantly impacts the power conversion efficiency and photostability.

Corroborated by density functional theory (DFT) simulations, this study unveils the impact of intentional metal doping on the optical properties of mixed halide perovskite and provides valuable insights into the development of advanced optoelectronic applications.

Figure 1a shows the atomic coordinates of Cs, Pb, I, and Br elements in the cubic perovskite phase of CsPbIBr_2 with the $Pm\bar{3}m$ space group. The structure shows a 6-fold coordination octahedron and the divalent cation Pb^{2+} surrounded by four Br^- and two I^- anions and the Cs^+ cation between them. Since Pb atoms donate 2 electrons to anions, it leads to the formation of a 2+ valence state. To intentionally control the valence states in doping, three kinds of metal ions, including Ag^+ , Zn^{2+} , and Sb^{3+} were added to CsPbIBr_2 precursor solutions to substitute Pb^{2+} cation, which is supposed to tune the doping type (p-type doping, intrinsic doping, and n-type doping) and density of electrical carriers. The film deposition details are given in the experimental section.

The structure and properties of the four types of films were thoroughly characterized and compared. The surface morphology of perovskite films is known to be closely correlated with PL behaviors and photovoltaic performance.³⁵ As shown in Figure 1b, the scanning electron microscopy (SEM) images indicate that all perovskite films are densely covered with very similar sizes of crystalline grains, suggesting that compositional modulation does not lead to a noticeable difference in the surface morphology. To examine the element distribution, energy dispersive X-ray (EDX) mapping was conducted on four types of films. As shown in Figure 1c–i, all elements, including Cs, Pb, I, and Br in the pristine film and doped elements (Ag, Zn, and Sb) in the corresponding films, are distributed evenly on the surface of halide perovskites, indicating that the physical properties, including the phase segregation behaviors discussed below, are not location dependent.^{27,36} Additionally, X-ray photoemission spectroscopy (XPS) measurements were carried out on these films after surface etching of 20 s to determine their atomic ratios. Figure S1a exhibits the whole spectra of four types of films, and Figure S1b–h demonstrate the Cs, Pb, I, Br, Ag 3d, Zn 3p, and Sb 3d spectra, respectively. It is shown that atomic ratios of Ag, Zn, and Sb are 0.91%, 0.90%, and 0.92%, respectively, which are very close to their nominal doping concentration of 1% in precursor solutions.

X-ray diffraction (XRD) measurements were performed on all perovskite films to characterize their crystal structures. Doped elements can modulate the lattice distance due to the partial substitution of Pb atoms by the others with different atomic radii compared with the Pb. As illustrated in Figure 2a, the main XRD peaks located at 15.06° and 30.08° can be attributed to the [100] and [200] planes of the cubic (α) phase of perovskite CsPbIBr₂, indicating that the phase and preferential growth direction in all CsPbIBr₂ films remained the same.²⁷ Notably, impurity peaks are not observed in all doped films, indicating that all CsPbIBr₂ samples with doped metal atoms were pure-phase perovskites with cubic structures. Additionally, it is observed that all peaks in the doped films shift to larger angles (see Figure 2b), suggesting the occurrence of lattice shrinking since the cation radii of all doped metal elements are smaller than that of Pb²⁺ (cation radii: Pb:120 pm, Ag:115 pm, Zn:74 pm, and Sb:76 pm).³⁷ The XRD results imply that impurity elements were successfully doped into CsPbIBr₂ perovskite structures. Furthermore, the peak intensities in all films are similar, implying that the crystallinity is not changed by doping. The XRD patterns were further analyzed using the Debye–Scherrer equation to determine the average grain sizes.³⁸ The obtained average grain sizes are 200.3 nm for the pristine film, 192.8 nm for the AgI–CsPbIBr₂ film, 208.5 nm for the ZnI₂–CsPbIBr₂ film, and 193.1 nm for the SbI₃–CsPbIBr₂ film, which are in good accordance with the SEM observation. The ultraviolet–visible (UV–vis) absorption spectra of four samples are shown in Figure 2c. One can see that the doped CsPbIBr₂ films exhibited slight changes in the absorption edge and the bandgaps can be calculated from the Tauc plots. The pristine film has a bandgap of 2.05 eV; Ag-doped film showed a slightly enlarged bandgap of 2.08 eV, Zn-doped film demonstrated a very similar bandgap of 2.04 eV, and Sb-doped film delivered a small bandgap of 2.03 eV. All above bandgaps are in good agreement with the reported ones. The shifted bandgaps of doped perovskite films indicate that metal atoms have been successfully induced into lattices, which

modified the interactions with the ions in the metal-halide networks.^{39,40}

Subsequently, steady-state PL measurements were carried out on four kinds of perovskite films, as shown in Figure 2d. Since defect trap states in perovskite films can cause nonradiative recombination, a stronger PL intensity generally indicates a lower defect density. The AgI–CsPbIBr₂ film owns the highest PL intensity, which is followed by the ZnI₂-doped film, the pristine film, and the SbI₃-doped film, suggesting that the trap density gradually increases in this order. Additionally, PL peak in AgI-doped, ZnI₂, and SbI₃ films demonstrated noticeable blue-shift, very slight red-shift, and noticeable red-shift, respectively, compared to that in the pristine film. To further verify the effect of trap density, carrier dynamics of perovskite films were studied by time-resolved PL (TRPL) decay (Figure 2e). The extracted carrier lifetimes, τ_1 representing nonradiative recombination and τ_2 representing intrinsic radiative recombination, are given in Table 1 using a

Table 1. Lifetimes of Four Types of Halide Perovskite Films

| lifetime | pristine | AgI | ZnI ₂ | SbI ₃ |
|----------|----------|-----|------------------|------------------|
| τ_1 | 1.4 | 1.8 | 1.2 | 0.9 |
| τ_2 | 8.9 | 9.7 | 8.8 | 7.3 |

biexponential decay function fitting. The lifetime τ_1 in AgI-doped film is prolonged and in ZnI₂-doped film is nearly the same, while that in the SbI₃–CsPbIBr₂ film is reduced compared with the pristine film, indicating that the defect density is suppressed after AgI, similar in ZnI₂ doping, and increased after SbI₃ introduction. This trend is in accordance with the steady-state PL results.

To further confirm the impact of doping on the defect characteristics, space-charge limited current (SCLC) measurements were performed on four types of films using a structure of ITO/SnO₂/perovskite/PCBM/Ag. As shown in Figure S2, the trap-filled limit voltage (V_{TFL}) is 0.54 V for the Ag-doped film, 0.85 V for the pristine film, 0.87 V for the Zn-doped film, and 1.03 V for the Sb-doped film. The number of electron trap density (n_{trap}) can be calculated according to $n_{\text{trap}} = \frac{2V_{\text{TFL}}}{eL^2} \epsilon \epsilon_0$, where L is the perovskite film thickness (100 nm); ϵ is the dielectric constant of CsPbIBr₂ (≈ 8); ϵ_0 is the vacuum permittivity; e represents the elementary charge.²⁷ The calculated trap densities are 7.52×10^{16} , 4.78×10^{16} , 7.70×10^{16} , and 9.12×10^{16} cm⁻³ for the pristine, Ag, Zn, and Sb-doped films, respectively. We should note that the exact defect densities estimated from the SCLC measurements may not be accurate due to ion migration and other factors, but it is reliable to reveal the relative trend among the films.^{41,42} Therefore, the trap density is reduced in Ag-doped film, similar in the pristine and the Zn-doped films, and increased in Sb-doped film. This trend is in good agreement with the PL results.

Ultraviolet-photoelectron spectroscopy (UPS) measurements were carried out on four types of films after the surface etching of 20 s to examine the energy levels. Figure S3a and S3b show the UPS spectra of perovskites in the cutoff and valence band edge regions, respectively. The Fermi level (E_{F}) can be determined using $E_{\text{F}} = 21.22 - E_{\text{cutoff}}$ while the valence band maximum (VBM) can be calculated by $\text{VBM} = 21.22 - (E_{\text{cutoff}} - E_{\text{onset}})$. To eliminate the errors associated with UPS measurement, 3 spots on the same films for each film were

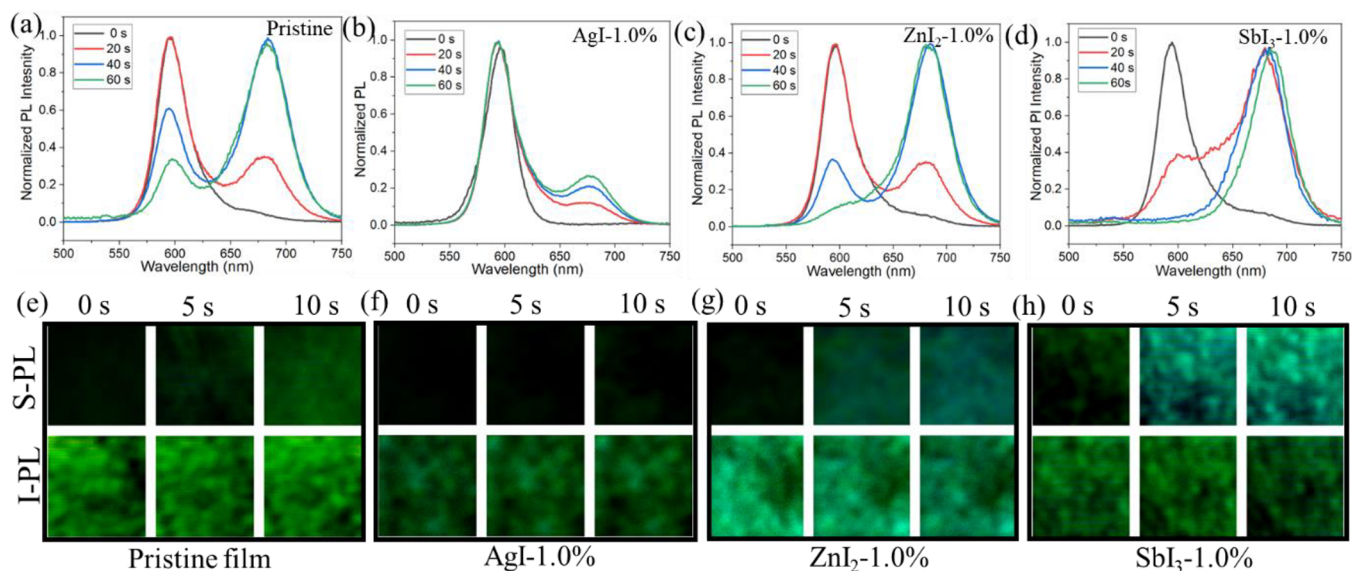


Figure 3. PL spectra results for (a) the pristine CsPbI₂Br₂ film, (b) the AgI-doped film, (c) ZnI₂-doped film, and (d) SbI₃-doped film. PL mapping of (e) pristine CsPbI₂Br₂ film, (f) the AgI-doped film, (g) ZnI₂-doped film, and (h) SbI₃-doped film in the wavelength ranges of 550–630 nm (original phase, I-PL) and 665–750 nm (segregated phase, S-PL), image size: 5 × 5 μm.

tested, which demonstrated the same trends in all spots for each sample as shown in Table S1. Then, by combining the bandgap of all films as shown in Figure S3c, the conduction band minimum (CBM) can be obtained. Figure 2f summarizes the obtained energy levels for four different perovskite films based on measurements on spot 1, which shows the impact of metal doping on the electronic band structure. The intrinsic material (pristine CsPbI₂Br₂) is n type due to the halide vacancy defects with low formation energy, which results in that Pb atoms would release free electrons producing n-type characteristics.¹⁴ The pristine and Zn-doped films demonstrate very similar band structure including CBM, VBM and Fermi level as well as n-type characteristics, while the Sb-doped film exhibits the downshift of CBM and VBM as well as enhanced n-type features and Ag-doped film delivers the upshift of CBM and VBM as well as an intrinsic physical property, which are consistent with the reported results.³³ Therefore, we can conclude that metal doping plays the deterministic role in altering the physical properties of the perovskite CsPbI₂Br₂ films, and we further hypothesize that it may modify the phase segregation behaviors under continuous illumination, which will be discussed later.

To investigate the effect of electronic properties on phase segregation, time-dependent PL was performed on four types of perovskite films. Under continuous illumination conditions, CsPbBrI₂ films with uniform bandgap can lead to the formation of I-rich domains and Br-rich domains due to the ion movement, and photogenerated holes and electrons would inject into small-bandgap I-rich domains, resulting in red-shifted PL emission. As shown in Figure 3a–d, the intrinsic PL peaks of four films are initially located between 580 and 600 nm. Then, the PL properties of all perovskite films were recorded with the duration of 0, 20, 40, and 60 s under the illumination of a 532 nm laser with an intensity of 10 mW/cm². The PL spectra were normalized to compare their features, in which two wavelength ranges of PL emission, namely 550–630 nm (intrinsic PL, named as I-PL) and 665–750 nm (phase-segregation induced PL emission, named as S-PL), were monitored simultaneously. Figure 3a presents the

PL evolution of pristine film, where the I-rich PL peak emerges at 20 s and its intensity continuously increases with time. On the other hand, Figure 3b shows that phase-segregated PL peaks (>665 nm) of AgI-doped film were substantially suppressed compared with that of the pristine film, evidencing that halide segregation was mitigated. In contrast, the PL characteristics of both ZnI₂ and SbI₃-doped CsPbI₂Br₂ films demonstrated faster phase segregation into I-rich domains (Figure 3c,d), and the intensity of I-rich emission is higher than that in pristine and AgI-doped films. These results point out that the phase segregation behavior is accelerated with the presence of Zn and Sb atoms. In addition, fluorescence imaging was performed on four types of films to visualize the phase segregation process under continuous illumination. As shown in Figure 3e–h corresponding to pristine, AgI-, ZnI₂-, and SbI₃-doped films, respectively, it is clear that phase segregation is significantly suppressed in the AgI-doped film since the PL located at the range of 665–750 nm was not detected at the time of 5 and 10 s, while the I-rich PL emission quickly emerges across the other three films under the same illumination condition. These results are consistent with the PL emission spectra shown in Figure 3a–d.

The overall phase segregation behaviors of pristine, AgI-, ZnI₂-, and SbI₃-doped CsPbI₂Br₂ films were monitored under continuous illumination, and the results are summarized in Figure S4. The intensity of saturated I-rich PL emission (fully segregated) is denoted as I_{sat} while I_{exp} represents the I-rich PL intensity at certain monitored times. One can see that the AgI-CsPbI₂Br₂ film exhibits the lowest emission intensity from segregated I-rich domains, confirming its high photostability against light-induced phase segregation. On the other hand, the ZnI₂-doped specimen reveals comparable segregation properties to the pristine CsPbI₂Br₂, while the SbI₃-doped film rapidly segregates and reaches I_{sat} implying unchanged and inferior photostability, respectively.

To further investigate the effect of Ag doping concentration on PL properties, four Ag-doped CsPbI₂Br₂ films with the molar concentrations of 0.1%, 0.5%, 1.0%, and 2.0% in precursor solutions were deposited. Figure 4a–d show the

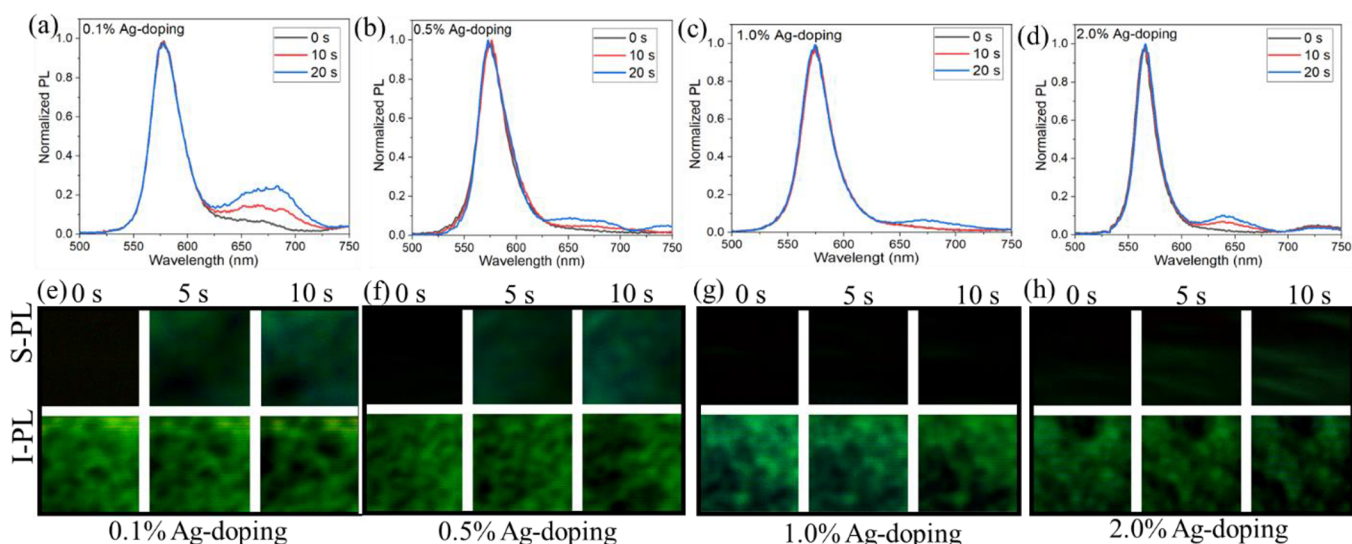


Figure 4. PL spectra for (a) the 0.1% AgI-doped film, (b) the 0.5% AgI-doped film, (c) 1.0% AgI-doped film, and (d) 2.0% AgI-doped film. PL mapping of (e) the 0.1% AgI-doped film, (f) the 0.5% AgI-doped film, (g) the 1.0% AgI-doped film, and (h) 2.0% AgI-doped film in the wavelength ranges of 550–630 nm (original phase, I-PL) and 665–750 nm (segregated phase, S-PL), image size: $5 \times 5 \mu\text{m}$.

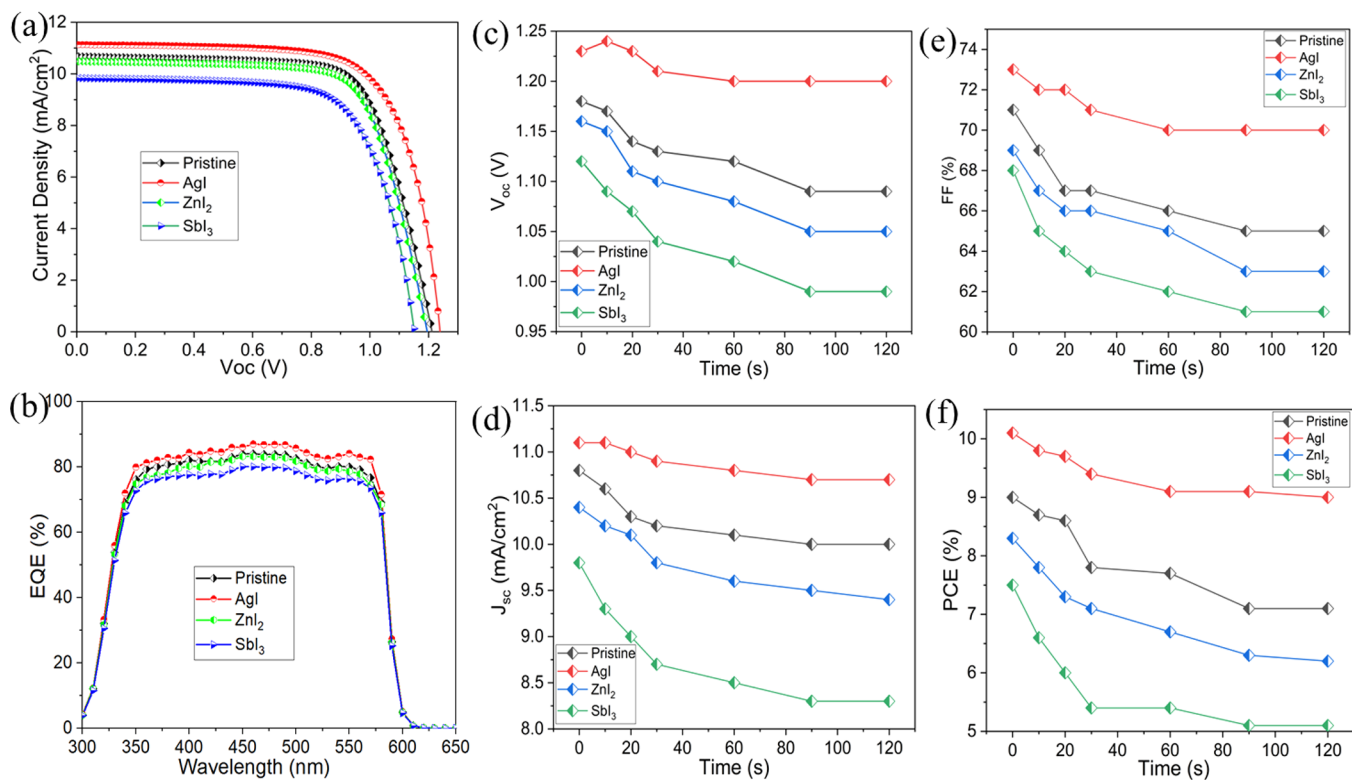


Figure 5. (a) J - V curves (b) EQE curves of pristine, AgI-, ZnI_2 -, and SbI_3 -doped CsPbI_3 solar cells. Detailed (c) V_{oc} , (d) J_{sc} , (e) FF, and (f) PCE performance over time for pristine, AgI-, ZnI_2 - and SbI_3 -doped CsPbI_3 solar cells under continuous solar irradiation.

normalized PL spectra of CsPbI_3 films under continuous light illumination with the duration time of 0, 10, and 20 s. It is clear that S-PL intensity was suppressed with the doping concentration increasing from 0.1% to 1.0%, while it slightly increased when the doping concentration increased to 2.0%. The corresponding PL mapping spectra further validated these trends. As shown in Figure 4e–h, increased S-PL mapping intensity was observed under the continuous light illumination at the time of 0, 5, and 10 s in the samples of 0.1%, 0.5%, and 2.0% Ag doping. In contrast, the S-PL mapping intensity in the

1.0% Ag-doped sample remained nearly the same. This result indicates that the Ag-doped samples with low doping concentrations of 0.1% and 0.5% still have notable densities of defects despite the beneficial doping effect, while at the highest Ag doping concentration of 2.0%, the excessive substitutions at the metal cation sites might create some degree of lattice defects.⁴³ The concentration-dependent result indicates that the 1.0% Ag-doped film has the optimal doping level and the best photostability among the four types of Ag-doped films.

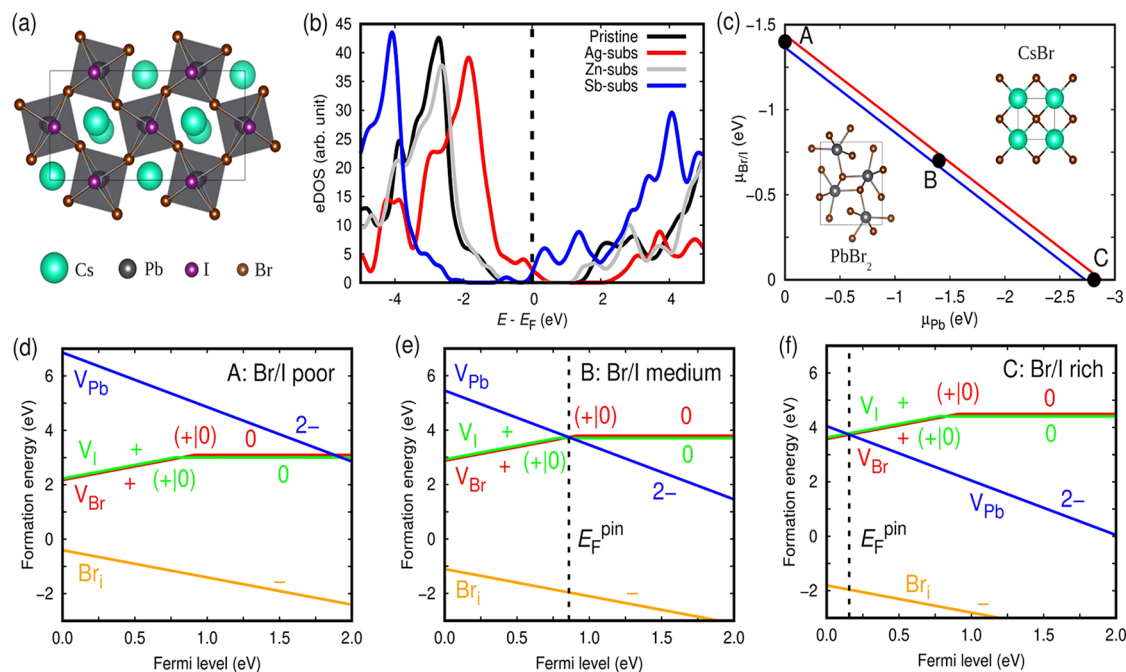


Figure 6. First-principles calculations based on density functional theory (DFT). (a) Sketch of the 40-atom supercell employed in the DFT calculations. (b) Density of electronic states (eDOS) of pristine CsPbI₃ and doped CsPbI₃ estimated with the DFT screened hybrid exchange-correlation potential HSE06;⁴⁴ the Fermi energy level has been shifted to zero in all the cases. (c) Estimation of chemical potentials for the Pb and Br/I species in CsPbI₃. Native defect equilibrium of CsPbI₃ calculated with DFT methods under (d) Br/I poor synthesis conditions, (e) Br/I medium synthesis conditions, and (f) Br/I rich synthesis conditions; the dashed vertical line in (e) and (f) represents the Fermi energy level pinned by the charge neutrality condition.

Based on the above results, four types of halide perovskite films including the pristine films (without metal element doping) and the films with the 1.0% doping concentration of Ag, Zn, and Sb elements were prepared and used to further investigate the effect of valence-controlled doping on solar cell performance under continuous light illumination. The device architecture is ITO/SnO₂/perovskite/Spiro/Au in four types of solar cells, and Figure S5 shows the cross-sectional SEM image of the Ag-doped CsPbI₃ solar cell. Figure 5a illustrates the current density–voltage (*J*–*V*) curves for four types of solar cells. AgI-CsPbI₃ solar cell features the best photovoltaic performance, which can be attributed to the lowest trap density as discussed above. With AgI doping, the photovoltaic power conversion efficiency (PCE) is significantly improved from 9.0% of the pristine sample to 10.1%, unambiguously demonstrating the benefit of AgI doping. However, Zn- and Sb-doped solar cells delivered inferior performances with PCEs of 8.4% and 7.6%, respectively. All parameters were improved after Ag doping, and they remained almost the same after Zn doping and decreased after Sb doping. The statistics of device performance of four types of solar cells are given in Table S2 (21 devices for each type of solar cell), showing that the average device parameters are consistent with the trends demonstrated in Figure 5a. Figure 5b shows the external quantum efficiency (EQE) of four types of solar cells, and the integrated current density (*J*_{sc}) from EQE test is 10.1, 10.6, 9.5, and 9.2 mA/cm² for pristine, Ag-, Zn-, and Sb-doped solar cells, respectively, well matched with their corresponding *J*–*V* results.

The photostability of four types of solar cells was monitored under continuous solar illumination (AM 1.5G, 100 mW/cm²) and their detailed photovoltaic parameters, including open voltage (*V*_{oc}), *J*_{sc} fill factor (FF), and PCE, are presented in

Figure 5c–f. Overall, the AgI-CsPbI₃ solar cell reveals the smallest decrease over time in all parameters. For example, the AgI-CsPbI₃ cell demonstrates 10.9% decay in PCE performance (from 10.1% to 9.0%) after 120 s of illumination, outperforming the pristine cell with 21.1% of PCE degradation (from 9.0% to 7.6%); and the decrease is 22.6% for the Zn-doped solar cell (8.4% to 7.4%) and 32.2% for the Sb-doped cells (7.6% to 5.1%). Apparently, Ag-doped solar cells demonstrated the best photostability. Since light-induced phase segregation is usually reversible, four kinds of solar cells were put in a drybox at dark for 3 h and their photovoltaic performances were tested again. As shown in Figure S6, the *J*–*V* characteristics and PCEs of four types of solar cells almost recovered to their initial levels, which demonstrated that the decreased performances in Figure 5b–f result from phase separation but not from the material degradation.

The improved photostability of AgI-CsPbI₃ solar cell demonstrated here can be explained by their charge transport characteristics. In this comparative study, the substitution of Pb by the valence-regulated doping elements resulted in distinct carrier properties, that is, the monovalent Ag, divalent Zn, and trivalent Sb led to p-type, intrinsic type, and n-type doping effects, respectively. With monovalent Ag p-doping, the Fermi level of CsPbI₃ is pulled down to the middle of the bandgap, and the perovskite features more intrinsic carrier properties than the pristine n-type sample. The intrinsic carrier characteristics in perovskite can help prevent the formation of defect trap states, leading to a reduced defect density, in line with the TRPL result discussed above. Furthermore, a deeper Fermi level in perovskite film tends to produce a larger band-bending, which is the driving force for hole extraction from the perovskite layer.³ As a result of the reduced defect density and the improved hole collection efficiency, the AgI-CsPbI₃ solar

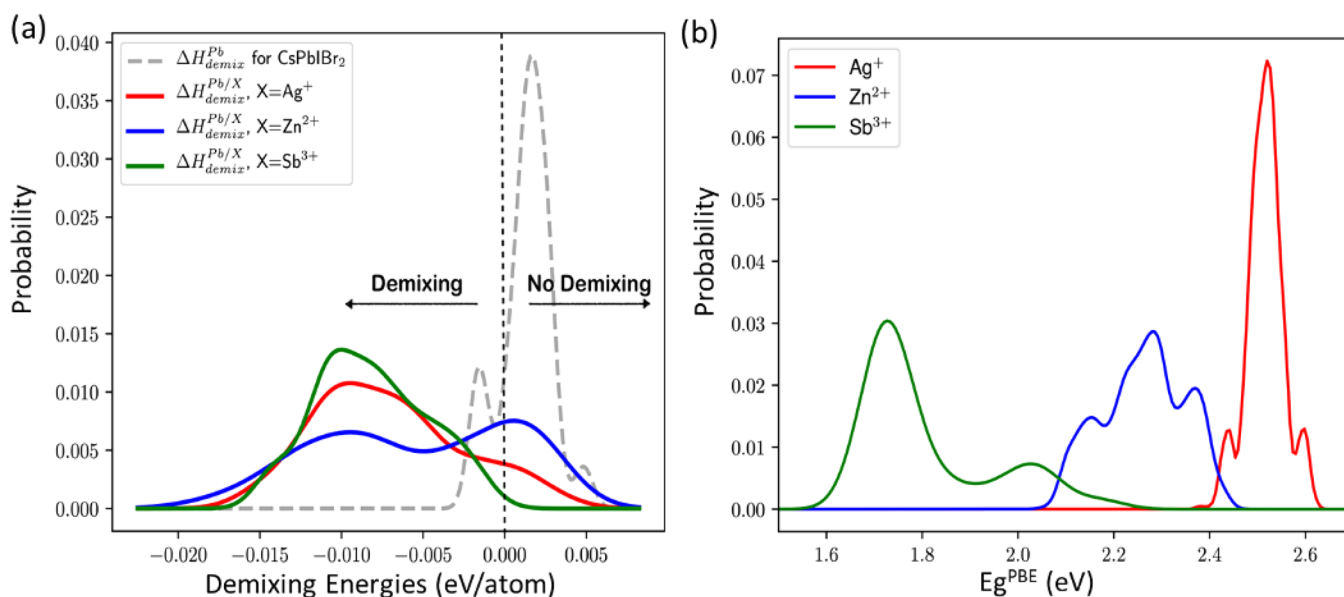


Figure 7. (a) Halide demixing enthalpy ($\Delta H_{\text{demix}}^{\text{Pb}}$) landscape, showing the distributions of $\Delta H_{\text{demix}}^{\text{Pb}}$ for CsPbIBr₂ and $\Delta H_{\text{demix}}^{\text{Pb}/\text{X}}$ for Cs(Pb_{0.875}X_{0.125})IBr₂ with X = Ag⁺, Zn²⁺ and Sb³⁺. (b) Distribution of the electronic band gap energies calculated for 1000 300 K-MD trajectory frames at PBE level of theory for Cs(Pb_{0.875}X_{0.125})IBr₂. All distributions have been smoothed with a kernel-density-estimate.

cell exhibits the best PCE of 10.1% among all studied devices. Additionally, after doping Ag atoms, the photostability of CsPbIBr₂ is remarkably improved against light-induced phase segregation because both the reduced trap density and intrinsic carrier environment help restrain unfavorable halide ion migration in the mixed halide perovskite. On the other hand, the divalent Zn, with equal valence to the Pb atom, provides a relatively intrinsic doping effect in the perovskite, which results in comparable phase segregation properties between ZnI₂-doped CsPbIBr₂ and pristine CsPbIBr₂. For trivalent Sb atoms, the extra electron can reinforce the n-type property of CsPbIBr₂, which not only promotes the formation of defect trap states but also accelerates light-induced phase segregation due to enhanced halide migration under high n-type doping conditions. Therefore, judicious doping with favorable properties in halide perovskites can notably boost the device performance and photostability.

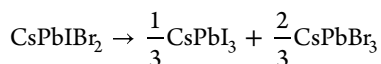
First-principles calculations based on density functional theory (DFT) were carried out to theoretically investigate the electronic properties of pristine and doped CsPbIBr₂ perovskites as well as the equilibrium of native defects in bulk CsPbIBr₂ (Figure 6).⁴⁵ The calculated energy bandgaps are in good agreement with the experimental measurements. In particular, we obtained 2.1, 2.0, 2.0, and 1.9 eV for pristine CsPbIBr₂ and Ag-, Zn-, Sb-doped CsPbIBr₂, respectively. The Pb-substitution-driven Fermi level shifts found in our DFT calculations qualitatively agree with the experimental results, namely, Ag-doping moves E_{F} toward the valence band (p-type), Sb-doping toward the conduction band (n-type) and Zn-doping produces negligible effect. There is a quantitative difference, however, between our DFT bandgap calculations and UPS measurements (i.e., a constant shift of roughly 0.5 eV) that we may ascribe to some composition differences between the simulated and real systems. In particular, the DFT bandgap results have been obtained for systems that are perfectly stoichiometric (i.e., do not contain point defects, in contrast to the real samples) and present doping concentrations of 12.5% (which are larger than the experimental ones,

due to obvious computational limitations on the number of atoms that can be accurately simulated).

To theoretically investigate how the changes in electronic structure may affect the equilibrium of native defects (i.e., Pb, I, and Br vacancies and Br interstitials) and optoelectronic performance of bulk CsPbIBr₂ at static state, we performed a series of DFT simulations considering different possible chemical potentials rendering I/Br poor, I/Br medium and I/Br rich synthesis conditions. For a defect to act as a nonradiative recombination center, a necessary condition is the existence of charge-state levels in the bandgap.⁴⁶ According to our DFT defect equilibrium calculations (Figure 6d–f), only I and Br vacancies (V_{I} and V_{Br}) can act as nonradiative recombination centers in CsPbIBr₂ since both types of defects present (+0) charge-state levels within the material bandgap. It is found that under the I/Br poor synthesis condition, no charge neutrality condition can be established; thus, the system becomes highly unstable against decomposition. Therefore, I/Br poor synthesis conditions, in contrast to I/Br medium and rich conditions, should be strongly avoided in practice. Meanwhile, under I/Br medium and rich conditions, the charge neutrality condition can be satisfied, and the pinning of the Fermi level occurs near the middle and bottom of the bandgap, respectively (Figure 6e,f). Given these results, one can understand the beneficial effect of Ag-doping: the E_{F} shift induced by such a Pb-substitution brings the Fermi level closer to its optimal pinning position, which confers stability to CsPbIBr₂. Conversely, Sb-doping moves the Fermi energy level away from its optimal location, thus unbalancing the system and weakening the stability. Furthermore, the formation energy of the two possible nonradiative defects, V_{I} and V_{Br} , is relatively high under I/Br medium and rich conditions, which implies that they should not be abundant in the samples. On the other hand, the formation energy of Br interstitials (Br_i) is always quite low, thus suggesting that this type of defect may be invariably abundant. This may accelerate light-induced halide segregation in all-inorganic halide perovskites, which was reported in previous works.^{47,48} Nevertheless, Br_i cannot

act as nonradiative recombination centers and consequently cannot detrimentally affect the optoelectronic properties of CsPbIBr₂. Therefore, in this work, we consider that I and Br vacancies (V_I and V_{Br}) act as nonradiative recombination centers in CsPbIBr₂ since both types of defects present (+10) charge-state levels within the material bandgap. This theoretical insight is in line with the improved optoelectronic performance observed for Ag-doped CsPbIBr₂.

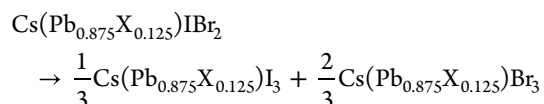
However, the thermodynamic and electronic properties of the defects alone may not be sufficient to fully explain the light-induced halide segregation behaviors in the doped CsPbIBr₂ systems. At the most fundamental level, the tendency of phase segregation should be dependent on the chemical bonding strengths, which in our case, can be modeled with the demixing enthalpy. For pristine CsPbIBr₂, this is defined for the chemical reaction of



as

$$\Delta H_{\text{demix}}^{\text{Pb}} = \frac{1}{3}E[\text{CsPbI}_3] + \frac{2}{3}E[\text{CsPbBr}_3] - E[\text{CsPbIBr}_2]$$

Similarly, for the doped system, the corresponding chemical reaction and demixing enthalpy are defined as



and

$$\begin{aligned} \Delta H_{\text{demix}}^{\text{Pb/X}} &= \frac{1}{3}E[\text{Cs}(\text{Pb}_{0.875}\text{X}_{0.125})\text{I}_3] \\ &+ \frac{2}{3}E[\text{Cs}(\text{Pb}_{0.875}\text{X}_{0.125})\text{Br}_3] \\ &- E[\text{Cs}(\text{Pb}_{0.875}\text{X}_{0.125})\text{IBr}_2] \end{aligned}$$

Here, E represents the total energy obtained from the DFT calculation. To obtain statistically significant results, a total of 26 configurations of CsPbIBr₂ and 570 configurations of Cs(Pb_{0.875}X_{0.125})I₃ across three different dopants have been sampled using the same random solid solution sampling approach as in our previous work.⁴⁹ Figure 7a shows the distributions of demixing energies for all systems considered.

The result in Figure 7a demonstrates that the Sb³⁺-doped CsPbIBr₂ is most prone to phase segregation, while the behaviors for Ag⁺- and Zn²⁺-doped samples are reversed. Most strikingly, halide demixing is found to be preferred in all three doped CsPbIBr₂ systems compared to the pristine CsPbIBr₂. This shows that the experimentally observed phase segregation behaviors cannot be fully explained with the strengths of chemical bonds at the static state. More specifically, light-induced phase segregation is a manifestation of the (dynamic) electron–phonon coupling effect in the solid state, in which systems with stronger electron–phonon coupling are more likely to incur phase segregation under light illuminations.² To illustrate this effect, we selected the most stable structure of Cs(Pb_{0.875}X_{0.125})I₃ for each X dopant as acquired from the DFT calculation, and we performed further *ab initio* molecular dynamic (MD) calculations at 300 K. Subsequently, we extracted 1000 frames from each MD trajectory and calculated

their associated electronic band gap energies at the PBE level of theory.

When atoms undergo thermal vibrations, the electronic orbital overlaps between neighboring atoms will change correspondingly, which results in changes in the band gap energies. A large (small) change in the orbital overlaps induced by the thermal vibrations will transfer to a large (small) change in the band gap energies, thus reflecting strong (weak) electron–phonon coupling strengths in the system. Computationally, this information can be obtained by examining the distribution of band gap energies that are sampled across the MD trajectory. As shown in Figure 7b, the electron–phonon coupling strengths, which are qualitatively proportional to the width of the band gap distributions, decrease in the order of Sb³⁺ > Zn²⁺ > Ag⁺. This follows nicely the halide segregation behaviors in these three samples observed experimentally, indicating they are significantly affected by the modifications in the electron–phonon coupling strengths as induced by three dopants with different valencies.

In summary, we used a suite of complementary experimental and theoretical tools to investigate the effect of valence-regulated metal doping on the phase segregation and the photovoltaic performance of mixed-halide perovskites. The structure and morphology of the perovskite films were not affected much by the metal doping, while the steady-state PL and TRPL measurements revealed that the trap densities in doped films are in the order of Ag < Zn < Sb. Additionally, the phase segregation properties of doped perovskite films under light illumination feature the same order, proving the superiority of Ag atomic doping to improve phase stability of mixed-halide perovskite film with reduced trap states. The Ag-doped CsPbIBr₂ solar cell possesses the best photovoltaic performance among all studied cells with the highest PCE of 10.1% and reinforced stability against photodegradation. The DFT simulations shed light on how valence-controlled metal doping shifts the Fermi level and affects the trap density of CsPbIBr₂ perovskites, as well as the modification in the electron–phonon coupling strengths that differentiate the halide segregation behaviors in the three doped materials. Overall, the study revealed that appropriate p-doping in n-type perovskites could deepen the Fermi level to the midgap and produce an unambiguously positive effect to suppress the defect states and promote the photostability, which provides insights into the development of high-quality mixed-halide perovskite in optoelectronic applications.

■ ASSOCIATED CONTENT

Supporting Information

The Supporting Information is available free of charge at <https://pubs.acs.org/doi/10.1021/acsenerylett.2c02040>.

- (1) Experimental section including chemicals and materials, mixed-halide perovskite precursor solution preparation, and mixed-halide perovskite films and solar cell fabrication; (2) Characterizations including TEM, SEM, PL, XPS, UPS, XRD, and UV–vis; (3) Theoretical calculations method including First-principles calculations based on density functional theory, random sampling of the solid solutions, structural optimization with density functional theory (DFT), and room-temperature structural and electronic dynamics; six figures and two tables (PDF)

■ AUTHOR INFORMATION

Corresponding Authors

Dewei Chu – School of Materials Science and Engineering, University of New South Wales (UNSW), Sydney, New South Wales 2052, Australia; orcid.org/0000-0003-4581-0560; Email: d.chu@unsw.edu.au

Claudio Cazorla – Departament de Física, Universitat Politècnica de Catalunya, E-08034 Barcelona, Spain; orcid.org/0000-0002-6501-4513; Email: claudio.cazorla@upc.edu

Jack Yang – School of Materials Science and Engineering, University of New South Wales (UNSW), Sydney, New South Wales 2052, Australia; orcid.org/0000-0003-3589-6807; Email: jianliang.yang1@unsw.edu.au

Shujuan Huang – School of Engineering, Macquarie University Sustainable Energy Research Centre, Macquarie University, Sydney, New South Wales 2109, Australia; orcid.org/0000-0003-3468-4773; Email: shujuan.huang@mq.edu.au

Tom Wu – School of Materials Science and Engineering, University of New South Wales (UNSW), Sydney, New South Wales 2052, Australia; orcid.org/0000-0003-0845-4827; Email: tom.wu@unsw.edu.au

Authors

Long Hu – School of Engineering, Macquarie University Sustainable Energy Research Centre, Macquarie University, Sydney, New South Wales 2109, Australia; School of Materials Science and Engineering, University of New South Wales (UNSW), Sydney, New South Wales 2052, Australia

Xinwei Guan – Global Innovative Centre for Advanced Nanomaterials, School of Engineering, College of Engineering, Science and Environment, The University of Newcastle, Callaghan, New South Wales 2308, Australia; orcid.org/0000-0002-0100-480X

Tao Wan – School of Materials Science and Engineering, University of New South Wales (UNSW), Sydney, New South Wales 2052, Australia; orcid.org/0000-0001-9345-8624

Chun-Ho Lin – School of Materials Science and Engineering, University of New South Wales (UNSW), Sydney, New South Wales 2052, Australia; orcid.org/0000-0003-0882-4728

Shanqin Liu – School of Chemistry and Chemical Engineering, Henan Institute of Science and Technology, Xinxiang, Henan 453003, P. R. China; orcid.org/0000-0003-4553-4922

Renbo Zhu – School of Materials Science and Engineering, University of New South Wales (UNSW), Sydney, New South Wales 2052, Australia

Weijian Chen – School of Photovoltaics and Renewable Energy Engineering, University of New South Wales (UNSW), Sydney, New South Wales 2052, Australia; orcid.org/0000-0001-8394-2391

Yin Yao – Electron Microscope Unit, Mark Wainwright Analytical Centre, UNSW Sydney, Sydney, New South Wales 2052, Australia

Chien-Yu Huang – School of Materials Science and Engineering, University of New South Wales (UNSW), Sydney, New South Wales 2052, Australia

Lin Yuan – School of Engineering, Macquarie University Sustainable Energy Research Centre, Macquarie University, Sydney, New South Wales 2109, Australia

Shamim Shahrokhi – School of Materials Science and Engineering, University of New South Wales (UNSW), Sydney, New South Wales 2052, Australia

Junfeng Chen – R&D Center, Shanghai Institute of Ceramics, Chinese Academy of Sciences, Shanghai 201899, P. R. China

Jiabao Yi – Global Innovative Centre for Advanced Nanomaterials, School of Engineering, College of Engineering, Science and Environment, The University of Newcastle, Callaghan, New South Wales 2308, Australia; orcid.org/0000-0001-5299-9897

Complete contact information is available at:

<https://pubs.acs.org/10.1021/acsenerylett.2c02040>

■ Author Contributions

▼ L.H., X.G., and T.W. equally contributed to this work.

■ Notes

The authors declare no competing financial interest.

■ ACKNOWLEDGMENTS

We acknowledge the support of the Australian Research Council (DP190103316). This project is partially supported by the Australian Renewable Energy Agency (ARENA) via Project 2020/RND001 and 2020/RND 003. C.C. acknowledges support from the Spanish Ministry of Science, Innovation, and Universities under the “Ramón y Cajal” fellowship RYC2018-024947-I. J. C. acknowledges the Science and Technology Commission of Shanghai Municipality, P.R. China under Grant 20511107402. J.Y. acknowledges the computational resource from the National Computing Infrastructures (NCI, project dy3), Australia, under the merit allocation schemes from the UNSW Research technology Services and NCI. This work used the facilities supported by Microscopy Australia at the Electron Microscope Unit at UNSW.

■ REFERENCES

- (1) Hoke, E. T.; Slotcavage, D. J.; Dohner, E. R.; Bowring, A. R.; Karunadasa, H. I.; McGehee, M. D. Reversible photo-induced trap formation in mixed-halide hybrid perovskites for photovoltaics. *Chem. Sci.* **2015**, *6* (1), 613–617.
- (2) Hu, L.; Guan, X. W.; Chen, W. J.; Yao, Y. C.; Wan, T.; Lin, C. H.; Pham, N. D.; Yuan, L.; Geng, X.; Wang, F.; et al. Linking Phase Segregation and Photovoltaic Performance of Mixed-Halide Perovskite Films through Grain Size Engineering. *ACS Energy Lett.* **2021**, *6* (4), 1649–1658.
- (3) Hu, L.; Duan, L.; Yao, Y.; Chen, W.; Zhou, Z.; Cazorla, C.; Lin, C. H.; Guan, X.; Geng, X.; Wang, F.; et al. Quantum Dot Passivation of Halide Perovskite Films with Reduced Defects, Suppressed Phase Segregation, and Enhanced Stability. *Adv. Sci.* **2022**, *9* (2), 2102258.
- (4) Mao, W.; Hall, C. R.; Bernardi, S.; Cheng, Y. B.; Widmer-Cooper, A.; Smith, T. A.; Bach, U. Light-induced reversal of ion segregation in mixed-halide perovskites. *Nat. Mater.* **2021**, *20* (1), 55–61.
- (5) Motti, S. G.; Patel, J. B.; Oliver, R. D. J.; Snaith, H. J.; Johnston, M. B.; Herz, L. M. Phase segregation in mixed-halide perovskites affects charge-carrier dynamics while preserving mobility. *Nat. Commun.* **2021**, *12* (1), 6955.
- (6) Brennan, M. C.; Draguta, S.; Kamat, P. V.; Kuno, M. Light-induced anion phase segregation in mixed halide perovskites. *ACS Energy Lett.* **2018**, *3* (1), 204–213.
- (7) Wang, Y. T.; Quintana, X.; Kim, J. Y.; Guan, X. W.; Hu, L.; Lin, C. H.; Jones, B. T.; Chen, W. J.; Wen, X. M.; Gao, H. W.; et al. Phase segregation in inorganic mixed-halide perovskites: from phenomena to mechanisms. *Photonics Res.* **2020**, *8* (11), A56–A71.

- (8) Kim, D. H.; Muzzillo, C. P.; Tong, J. H.; Palmstrom, A. F.; Larson, B. W.; Choi, C.; Harvey, S. P.; Glynn, S.; Whitaker, J. B.; Zhang, F.; et al. Bimolecular Additives Improve Wide-Band-Gap Perovskites for Efficient Tandem Solar Cells with CIGS. *Joule* **2019**, *3* (7), 1734–1745.
- (9) Gualdrón-Reyes, A. s. F.; Yoon, S. J.; Barea, E. M.; Agouram, S.; Muñoz-Sanjosé, V.; Meléndez, A. n. M.; Niño-Gómez, M. E.; Mora-Seró, I. n. Controlling the phase segregation in mixed halide perovskites through nanocrystal size. *ACS Energy Lett.* **2019**, *4* (1), 54–62.
- (10) Liang, J.; Chen, C.; Hu, X.; Chen, Z.; Zheng, X.; Li, J.; Wang, H.; Ye, F.; Xiao, M.; Lu, Z.; et al. Suppressing the Phase Segregation with Potassium for Highly Efficient and Photostable Inverted Wide-Band Gap Halide Perovskite Solar Cells. *ACS Appl. Mater. Interfaces* **2020**, *12* (43), 48458–48466.
- (11) Cho, J. S.; Kamat, P. V. How Chloride Suppresses Photoinduced Phase Segregation in Mixed Halide Perovskites. *Chem. Mater.* **2020**, *32* (14), 6206–6212.
- (12) Balakrishna, R. G.; Kobosko, S. M.; Kamat, P. V. Mixed Halide Perovskite Solar Cells. Consequence of Iodide Treatment on Phase Segregation Recovery. *ACS Energy Lett.* **2018**, *3* (9), 2267–2272.
- (13) Knight, A. J.; Wright, A. D.; Patel, J. B.; McMeekin, D. P.; Snaith, H. J.; Johnston, M. B.; Herz, L. M. Electronic traps and phase segregation in lead mixed-halide perovskite. *ACS Energy Lett.* **2019**, *4* (1), 75–84.
- (14) Fan, W. S.; Shi, Y. L.; Shi, T. F.; Chu, S. L.; Chen, W. J.; Ighodalo, K. O.; Zhao, J.; Li, X. H.; Xiao, Z. G. Suppression and Reversion of Light-Induced Phase Separation in Mixed-Halide Perovskites by Oxygen Passivation. *ACS Energy Lett.* **2019**, *4* (9), 2052–2058.
- (15) Mahesh, S.; Ball, J. M.; Oliver, R. D. J.; Mcmeekin, D. P.; Nayak, P. K.; Johnston, M. B.; Snaith, H. J. Revealing the origin of voltage loss in mixed-halide perovskite solar cells. *Energy Environ. Sci.* **2020**, *13* (1), 258–267.
- (16) Dang, H. X.; Wang, K.; Ghasemi, M.; Tang, M. C.; De Bastiani, M.; Aydin, E.; Dauzon, E.; Barrit, D.; Peng, J.; Smilgies, D. M.; et al. Multi-cation Synergy Suppresses Phase Segregation in Mixed-Halide Perovskites. *Joule* **2019**, *3* (7), 1746–1764.
- (17) Nandi, P.; Li, Z.; Kim, Y.; Ahn, T. K.; Park, N. G.; Shin, H. Stabilizing Mixed Halide Lead Perovskites against Photoinduced Phase Segregation by A-Site Cation Alloying. *ACS Energy Lett.* **2021**, *6* (3), 837–847.
- (18) Lin, C. H.; Hu, L.; Guan, X.; Kim, J.; Huang, C. Y.; Huang, J. K.; Singh, S.; Wu, T. Electrode Engineering in Halide Perovskite Electronics: Plenty of Room at the Interfaces. *Adv. Mater.* **2022**, *34* (18), 2108616.
- (19) Euvrard, J.; Yan, Y. F.; Mitzi, D. B. Electrical doping in halide perovskites. *Nat. Rev. Mater.* **2021**, *6* (6), 531–549.
- (20) Xiang, W.; Wang, Z.; Kubicki, D. J.; Wang, X.; Tress, W.; Luo, J.; Zhang, J.; Hofstetter, A.; Zhang, L.; Emsley, L.; et al. Ba-induced phase segregation and band gap reduction in mixed-halide inorganic perovskite solar cells. *Nat. Commun.* **2019**, *10* (1), 4686.
- (21) Zeng, Q.; Zhang, X.; Feng, X.; Lu, S.; Chen, Z.; Yong, X.; Redfern, S. A. T.; Wei, H.; Wang, H.; Shen, H.; et al. Polymer-Passivated Inorganic Cesium Lead Mixed-Halide Perovskites for Stable and Efficient Solar Cells with High Open-Circuit Voltage over 1.3 V. *Adv. Mater.* **2018**, *30* (9), 1705393.
- (22) Tian, J.; Xue, Q.; Tang, X.; Chen, Y.; Li, N.; Hu, Z.; Shi, T.; Wang, X.; Huang, F.; Brabec, C. J.; et al. Dual Interfacial Design for Efficient CsPbI₂ Br Perovskite Solar Cells with Improved Photostability. *Adv. Mater.* **2019**, *31* (23), 1901152.
- (23) Shen, E. C.; Chen, J. D.; Tian, Y.; Luo, Y. X.; Shen, Y.; Sun, Q.; Jin, T. Y.; Shi, G. Z.; Li, Y. Q.; Tang, J. X. Interfacial Energy Level Tuning for Efficient and Thermostable CsPbI₂Br Perovskite Solar Cells. *Adv. Sci.* **2020**, *7* (1), 1901952.
- (24) Lau, C. F. J.; Zhang, M.; Deng, X. F.; Zheng, J. H.; Bing, J. M.; Ma, Q. S.; Kim, J.; Hu, L.; Green, M. A.; Huang, S. J.; et al. Strontium-Doped Low-Temperature-Processed CsPbI₂Br Perovskite Solar Cells. *ACS Energy Lett.* **2017**, *2* (10), 2319–2325.
- (25) Xiang, W. C.; Wang, Z. W.; Kubicki, D. J.; Tress, W.; Luo, J. S.; Prochowicz, D.; Akin, S.; Emsley, L.; Zhou, J. T.; Dietler, G.; et al. Europium-Doped CsPbI₂Br for Stable and Highly Efficient Inorganic Perovskite Solar Cells. *Joule* **2019**, *3* (1), 205–214.
- (26) Yoon, S. J.; Draguta, S.; Manser, J. S.; Sharia, O.; Schneider, W. F.; Kuno, M.; Kamat, P. V. Tracking Iodide and Bromide Ion Segregation in Mixed Halide Lead Perovskites during Photoirradiation. *ACS Energy Lett.* **2016**, *1* (1), 290–296.
- (27) Liu, P.; Yang, X.; Chen, Y.; Xiang, H.; Wang, W.; Ran, R.; Zhou, W.; Shao, Z. Promoting the Efficiency and Stability of CsPbI₂Br₂-Based All-Inorganic Perovskite Solar Cells through a Functional Cu(2+) Doping Strategy. *ACS Appl. Mater. Interfaces* **2020**, *12* (21), 23984–23994.
- (28) Ho-Baillie, A.; Zhang, M.; Lau, C. F. J.; Ma, F. J.; Huang, S. J. Untapped Potentials of Inorganic Metal Halide Perovskite Solar Cells. *Joule* **2019**, *3* (4), 938–955.
- (29) Munday, J. N. The effect of photonic bandgap materials on the Shockley-Queisser limit. *J. Appl. Phys.* **2012**, *112* (6), 064501.
- (30) Li, W.; Rothmann, M. U.; Liu, A.; Wang, Z. Y.; Zhang, Y. P.; Pascoe, A. R.; Lu, J. F.; Jiang, L. C.; Chen, Y.; Huang, F. Z.; et al. Phase Segregation Enhanced Ion Movement in Efficient Inorganic CsPbI₂Br₂ Solar Cells. *Adv. Energy Mater.* **2017**, *7* (20), 1700946.
- (31) Long, Y.; Wang, C.; Liu, X.; Wang, J.; Fu, S.; Zhang, J.; Hu, Z.; Zhu, Y. Zinc ion functional doping for all-inorganic planar CsPbI₂Br₂ perovskite solar cells with efficiency over 10.5%. *J. Mater. Chem. C* **2021**, *9* (6), 2145–2155.
- (32) Knight, A. J.; Patel, J. B.; Snaith, H. J.; Johnston, M. B.; Herz, L. M. Trap States, Electric Fields, and Phase Segregation in Mixed-Halide Perovskite Photovoltaic Devices. *Adv. Energy Mater.* **2020**, *10* (9), 1903488.
- (33) Zhou, S.; Ma, Y. P.; Zhou, G. D.; Xu, X.; Qin, M. C.; Li, Y. H.; Hsu, Y. J.; Hu, H. L.; Li, G.; Zhao, N.; et al. Ag-Doped Halide Perovskite Nanocrystals for Tunable Band Structure and Efficient Charge Transport. *ACS Energy Lett.* **2019**, *4* (2), 534.
- (34) Nayak, P. K.; Sendner, M.; Wenger, B.; Wang, Z.; Sharma, K.; Ramadan, A. J.; Lovrincic, R.; Pucci, A.; Madhu, P. K.; Snaith, H. J. Impact of Bi(3+) Heterovalent Doping in Organic-Inorganic Metal Halide Perovskite Crystals. *J. Am. Chem. Soc.* **2018**, *140* (2), 574–577.
- (35) Zhou, Y.; Wang, F.; Cao, Y.; Wang, J. P.; Fang, H. H.; Loi, M. A.; Zhao, N.; Wong, C. P. Benzylamine-Treated Wide-Bandgap Perovskite with High Thermal-Photostability and Photovoltaic Performance. *Adv. Energy Mater.* **2017**, *7* (22), 1701048.
- (36) Zhang, B.; Bi, W.; Wu, Y.; Chen, C.; Li, H.; Song, Z.; Dai, Q.; Xu, L.; Song, H. High-Performance CsPbI₂Br₂ Perovskite Solar Cells: Effectively Promoted Crystal Growth by Antisolvent and Organic Ion Strategies. *ACS Appl. Mater. Interfaces* **2019**, *11* (37), 33868–33878.
- (37) Hong, D.; Zhao, P.; Du, Y.; Zhao, C.; Xia, Y.; Wei, Z.; Jin, Z.; Tian, Y. Inhibition of Phase Segregation in Cesium Lead Mixed-Halide Perovskites by B-Site Doping. *iScience* **2020**, *23* (8), 101415.
- (38) Kim, J.; Hu, L.; Chen, H. J.; Guan, X. W.; Anandan, P. R.; Li, F.; Tang, J. B.; Lin, C. H.; Kalantar-Zadeh, K.; Tricoli, A.; et al. P-type Charge Transport and Selective Gas Sensing of All-Inorganic Perovskite Nanocrystals. *ACS Mater. Lett.* **2020**, *2* (11), 1368–1374.
- (39) Chen, J. X.; Xu, X. F.; Ma, Y. Q.; Qin, H. J.; Liu, J.; Lv, F. Z.; Zhu, C. M.; Wang, L. G.; Long, L. Z.; Liu, F. C.; et al. Effects of pyridine-like and pyrrolic-like nitrogen on the photoluminescence blue-shift of nitrogen-doped graphene oxide quantum dots. *J. Lumin.* **2021**, *235*, 117983.
- (40) Ghaffarkhah, A.; Hosseini, E.; Kamkar, M.; Sehat, A. A.; Dordanihaghghi, S.; Allahbakhsh, A.; van der Kuur, C.; Arjmand, M. Synthesis, Applications, and Prospects of Graphene Quantum Dots: A Comprehensive Review. *Small* **2022**, *18* (2), 2102683.
- (41) Le Corre, V. M.; Duijnste, E. A.; El Tambouli, O.; Ball, J. M.; Snaith, H. J.; Lim, J.; Koster, L. J. A. Revealing Charge Carrier Mobility and Defect Densities in Metal Halide Perovskites via Space-Charge-Limited Current Measurements. *ACS Energy Lett.* **2021**, *6* (3), 1087–1094.
- (42) Duijnste, E. A.; Ball, J. M.; Le Corre, V. M.; Koster, L. J. A.; Snaith, H. J.; Lim, J. Toward Understanding Space-Charge Limited

Current Measurements on Metal Halide Perovskites. *ACS Energy Lett.* **2020**, *5* (2), 376–384.

(43) Lin, Y.; Shao, Y.; Dai, J.; Li, T.; Liu, Y.; Dai, X.; Xiao, X.; Deng, Y.; Gruverman, A.; Zeng, X. C.; et al. Metallic surface doping of metal halide perovskites. *Nat. Commun.* **2021**, *12* (1), 7.

(44) Brothers, E. N.; Izmaylov, A. F.; Normand, J. O.; Barone, V.; Scuseria, G. E. Accurate solid-state band gaps via screened hybrid electronic structure calculations. *J. Chem. Phys.* **2008**, *129* (1), 011102.

(45) Cazorla, C.; Boronat, J. Simulation and understanding of atomic and molecular quantum crystals. *Rev. Mod. Phys.* **2017**, *89* (3), 035003.

(46) Li, Y. F.; Zhang, C. H.; Zhang, X. X.; Huang, D.; Shen, Q.; Cheng, Y. C.; Huang, W. Intrinsic point defects in inorganic perovskite CsPbI₃ from first-principles prediction. *Appl. Phys. Lett.* **2017**, *111* (16), 162106.

(47) Motti, S. G.; Meggiolaro, D.; Martani, S.; Sorrentino, R.; Barker, A. J.; De Angelis, F.; Petrozza, A. Defect Activity in Lead Halide Perovskites. *Adv. Mater.* **2019**, *31* (47), 1901183.

(48) Frolova, L. A.; Luchkin, S. Y.; Lekina, Y.; Gutsev, L. G.; Tsarev, S. A.; Zhidkov, I. S.; Kurmaev, E. Z.; Shen, Z. X.; Stevenson, K. J.; Aldoshin, S. M.; Troshin, P. A. Reversible Pb²⁺/Pb⁰ and I⁻/I³⁻ Redox Chemistry Drives the Light-Induced Phase Segregation in All-Inorganic Mixed Halide Perovskites. *Adv. Energy Mater.* **2021**, *11* (12), 2002934.

(49) Yang, J.; wang, Y. T.; Wu, T.; Li, S. Correlating the Composition-Dependent Structural and Electronic Dynamics of Inorganic Mixed Halide Perovskites. *Chem. Mater.* **2020**, *32* (6), 2470–2481.